The Astronomical Journal, 133:2624–2629, 2007 June

SELF-GRAVITY WAKE STRUCTURES IN SATURN'S A RING REVEALED BY *CASSINI* VIMS

Matthew M. Hedman and Philip D. Nicholson
Department of Astronomy, Cornell University, Ithaca, NY 14853, USA

Heikki Salo
Astronomy Division, University of Oulu, Oulu FIN-90014, Finland

Bradford D. Wallis, Bonnie J. Buratti, and Kevin H. Baines
Jet Propulsion Laboratory, Pasadena, CA 91109, USA

Robert H. Brown
Lunar and Planetary Laboratory, University of Arizona, Tuscon, AZ 85721, USA

and

Roger N. Clark
US Geological Survey, Federal Center, Denver, CO 80225, USA
Received 2006 December 1; accepted 2007 February 26

ABSTRACT

During the summer of 2005, the Visual and Infrared Mapping Spectrometer onboard the *Cassini* spacecraft observed a series of occultations of the star o Ceti (Mira) by Saturn's rings. These observations revealed pronounced variations in the optical depth of the A ring with longitude, which can be attributed to oriented structures in the rings known as self-gravity wakes. While the wakes themselves are only tens of meters across and below the resolution of the measurements, we are able to obtain information about the orientation and shapes of these structures by comparing the observed transmission at different longitudes with predictions from a simple model. Our findings include the following: (1) The orientation of the wakes varies systematically with radius, trailing by between 64° and 72° relative to the local radial direction. (2) The maximum transmission peaks at roughly 8% for $B = 3.45°$ in the middle A ring (∼129,000 km). (3) Both the wake orientation and maximum transmission vary anomalously in the vicinity of two strong density waves (Janus 5:4 and Mimas 5:3). (4) The ratio of the wake vertical thickness H to the wake pattern wavelength λ (assuming infinite, straight, regularly-spaced wake structures) varies from 0.12 to 0.09 across the A ring. Gravitational instability theory predicts $\lambda \sim 60$ m, which suggests that the wake structures in the A ring are only ∼6 m thick.

Key words: planets: rings

Online material: color figures

1. INTRODUCTION

Stellar occultations are a powerful tool for studying ring systems. The first complete radial profile of the optical depth of Saturn's rings was provided by a stellar occultation observed by the *Voyager 2* spacecraft in 1981 (Holberg et al. 1982; Lane et al. 1982; Esposito et al. 1983a). These data played an important role in the discovery and characterization of density waves in the rings (Holberg et al. 1982); several narrow, eccentric ringlets (Esposito et al. 1983b; Porco et al. 1984); and the wakes produced by a satellite orbiting within a gap in the rings (Showalter et al. 1986). Subsequent ground-based observations of an occultation by the star 28 Sgr helped establish an absolute radial scale for the rings accurate to ∼1 km (French et al. 1993). These data have even contributed information about the particle size distribution in the rings (Showalter & Nicholson 1990; French & Nicholson 2000). Over the 4 yr duration of the prime *Cassini* mission, approximately 100 stellar occultations are planned, which should make major contributions to our understanding of Saturn's rings. We report here on a series of occultations of the star o Ceti (Mira) observed by the Visual and Infrared Mapping Spectrometer (VIMS) onboard the *Cassini* orbiter. These occultations were obtained while the ring opening angle to the spacecraft was only 3.45°, and were designed to observe low optical depth regions such as the F ring and Cassini's division at high signal-to-noise ratio (this aspect of these observations will be discussed in later papers). However, these observations also yielded some unexpected information about the fine-scale texture of the A ring. While the measured transmission through most of the A ring was only a few percent, we were surprised to find that the signal transmitted through the rings at a given radius could vary by as much as a factor of 8 depending on the longitude of the occultation track relative to the spacecraft.

Similar azimuthal asymmetries in the rings have been detected in reflected and transmitted sunlight (Thompson et al. 1984; Lumme & Irvine 1984; Franklin et al. 1987; Dones et al. 1993; French et al. 2007), radar echoes (Nicholson et al. 2005), thermal emission (Ferrari et al. 2005), and most recently in other stellar occultations (Colwell et al. 2006). All of these asymmetries are attributed to the presence of elongated, regularly spaced aggregations of ring particles that have a characteristic trailing orientation of ∼20° relative to the local direction of orbital motion. These structures, called self-gravity wakes, are too small (∼50 m across) to be be directly observed. However, they are a robust prediction of analytic theory and numerical simulations (Julian & Toomre 1966; Salo 1995; Salo et al. 2004 and references therein), where they arise from a combination of mutual gravitational attraction between ring particles and Keplerian shear.

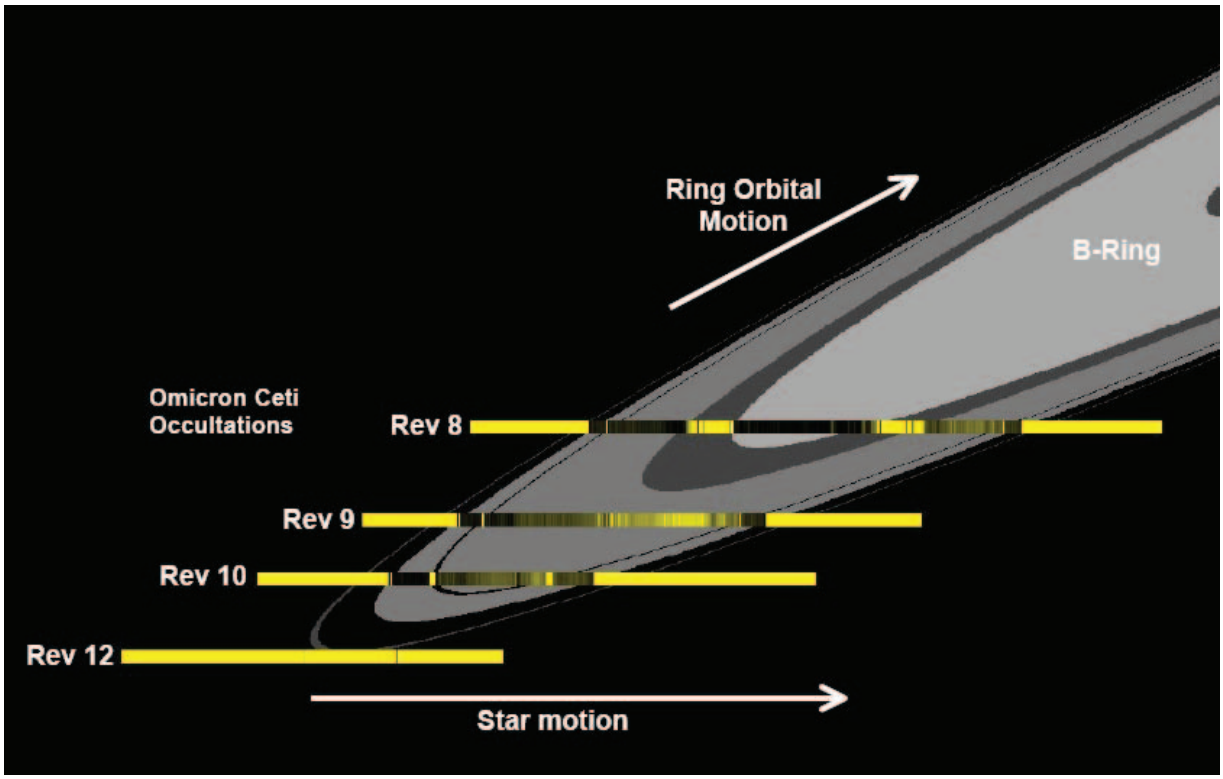

FIG. 1.—Summary of the geometry of the o Ceti occultations. The background images show the orientation of the F, A, and B rings during the time of the observations. The yellow bands show the track of the star as seen by *Cassini* on different orbits. The brightness in these bands is proportional to the observed transmission through the rings. Note that the transmission is systematically higher on the right (trailing) side of the rings.

Beyond providing further indirect evidence for these structures, the VIMS o Ceti occultations provide important new constraints on the shapes and geometries of the self-gravity wakes. A previous analysis of occultation data obtained by *Cassini*'s UVIS instrument (Colwell et al. 2006) fit data from multiple stars to a simple six-parameter model of the wakes. This study found that the ratio of the wake thickness to the wake width H/W ranges between 0.15 and 0.37, the ratio of the interwake spacing to the wake thickness G/H ranges between 6.8 and 7.7, and the optical depth of the spaces between the wakes varies between 0.1 and 0.3. However, since this analysis involved a global fit to occultation data from multiple stars, there is not a straightforward relationship between the observables and the model parameters.

By contrast, the VIMS o Ceti occultations all involve a single star and the same ring opening angle to the spacecraft, so the relevant data set is much more homogeneous. This limits the number of parameters we can constrain, but enables us to directly connect a few parameters to measurable quantities, greatly simplifying the interpretation. Furthermore, one of the parameters we can measure well is the orientation of the wakes, which the UVIS observations could only estimate to within 4°–5°.

2. OBSERVATIONS

VIMS is most often used to produce spatially resolved spectra of planetary targets between 0.3 and 5.1 μm. However, VIMS is a flexible instrument that can operate in a variety of modes, including an occultation mode (Brown et al. 2004). In this mode, the imaging capabilities are disabled, the short-wavelength VIS channel of the instrument is turned off, and the IR channel obtains a series of 0.8–5.1 μm spectra from a single pixel targeted at a star. A precise time stamp is appended to every spectrum to facilitate reconstruction of the occultation geometry.

The o Ceti occultations used an 80 ms integration time with negligible gaps between sequential spectra, which corresponds to a sampling distance of 1.3 km in the ring plane. This is comparable to the apparent stellar diameter (800 m) at the spacecraft-Saturn distance of approximately 1.6×10^6 km. The effective radial resolution of each scan ranges between 400 m and 4 km because the projected radial components of the occultation track and the direction to the star change as a function of radius. We did not expect to observe narrow spectral features in the occultation data, so the normal spectral resolution of the instrument was reduced by a factor of 8 to reduce data volume. A total of 32 spectral channels were returned with $\Delta\lambda \simeq 0.14$ μm.

Figure 1 summarizes the geometry of the relevant observations. The line of sight to the star is inclined by only 3.45° to the ring plane, and all the occultations cut obliquely through the same ring ansa. The first observation on orbit 8 penetrated the furthest, reaching the outer edge of the B ring. Due to small shifts in the spacecraft orbit, subsequent occultations on orbits 9 and 10 only penetrated as far as the A ring, while the last occultation on orbit 12 only cut across the F ring.

For each occultation, the available SPICE kernels provided by the *Cassini* navigation team were used to predict where the apparent position of the star in the ring plane should have been as a function of time. This preliminary estimate of the occultation geometry was refined using gap edges in Cassini's division and the outer A Ring (features 1, 3, 4, 13, 16, and 20 of French et al. 1993). We were able to align all of the observed features in the occultations with their predicted positions using three adjustable parameters: (1) an offset of the scan along the direction of the nominal track, quantified as a shift in the occultation timing; (2) an offset in the occultation perpendicular to the nominal track direction; and (3) a rotation about the nominal track orientation. The required adjustments were (1) less than

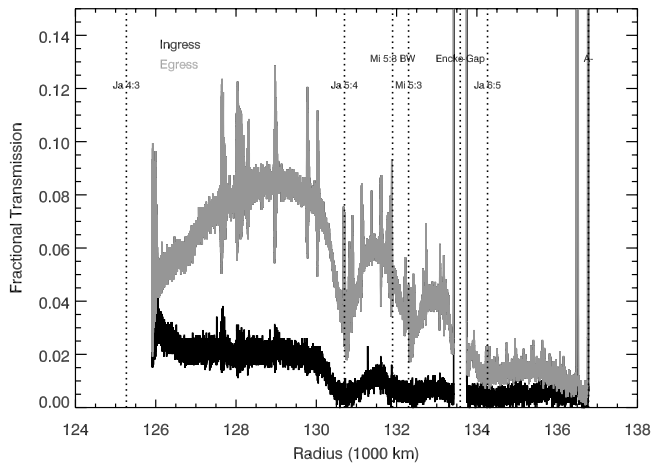

FIG. 2.—Light curve for the orbit 9 occultation, showing the transmission as a function of radius (median-filtered to remove cosmic-ray spikes). Note that transmission measured during ingress (*black*) is significantly lower than the transmission measured during egress (*gray*). The localized regions of increased variance in the egress profile correspond to density and bending waves in the A ring. The locations of the strongest Lindblad and vertical resonances in this region are indicated by dotted lines (Mi, Mimas; Ja, Janus), along with the Encke Gap and the outer edge of the A ring. [*See the electronic edition of the Journal for a color version of this figure*.]

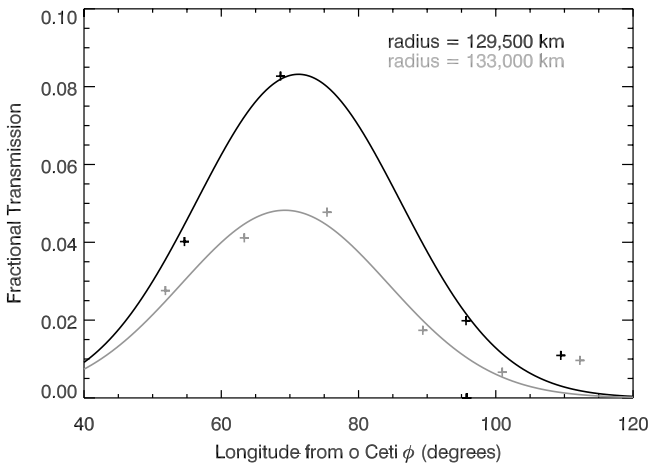

FIG. 3.—Measured transmission at 129,500 and 133,000 km as a function of longitude relative to the stellar direction. The curves are Gaussian fits to the data. Note that there are only four occultation cuts for radii less than 132,000 km. Each data point corresponds to an average transmission over 20 km in orbital radius and has a statistical uncertainty of order 0.0004. [*See the electronic edition of the Journal for a color version of this figure*.]

two minutes, (2) 20–100 km, and (3) less than 0.2° in all cases, within the uncertainty of the preliminary track.

The data used in this analysis are uncalibrated, but a mean instrumental thermal background has been subtracted from the spectra. During part of each occultation, the star passed near or behind illuminated portions of the rings, so the signal measured by the VIMS instrument was a combination of transmitted starlight and reflected sunlight. The reflected signal from the rings is strongly attenuated at wavelengths close to the strong 2.9 μm water ice absorption band, so we use the spectral channel corresponding to wavelengths between 2.87 and 3.00 μm in this analysis. In this channel, the reflected light from the rings is undetectable. We normalize the signal from the unocculted star to unity in the regions 138,000–139,000 and 141,000–142,000 km on either side of the narrow F ring. The baseline signal after each occultation was within 1% of the signal before the occultation, so we do not attempt to fit for any drift in baseline over the course of a single occultation.

3. CONSTRAINTS ON SELF-GRAVITY WAKE STRUCTURE

Owing to the small ring opening angle ($B = 3.45°$), the transmission through most of the A ring during the o Ceti occultations (assuming the ring could be treated as a uniform sheet of material) was expected to be negligible: $e^{-\tau/\sin B} \simeq 3 \times 10^{-4}$ for $\tau \sim 0.5$. In practice, the transmission through parts of the A ring was found to be as high as 8%. Furthermore, there were clear systematic variations in the measured transmission between different occultations and between ingress and egress within each occultation (see Fig. 2). The read noise per sample for these observations was approximately 0.003 in transmission, so these variations are well above the detector noise. These differences also cannot be attributed to instrumental artifacts (such as shifts in the background flux), because the scan with lower average transmittance also has more muted small scale features (such as strong density waves). The observed asymmetries in the occultation data therefore must reflect real variations in the optical depth of the A ring.

While the current VIMS occultation data cover only a limited range of longitudes, they reveal patterns consistent with those expected from self-gravity wakes. Figure 3 shows the measured transmission at two particular radii in the A ring as a function of inertial longitude in the ring plane measured relative to the longitude of the star, ϕ.[1] Our three occultations give us as many as six independent measurements of the transmission, which clearly indicate that the transmission peaks around $\phi = 70°$, where the projected filling factor of the wakes is expected to be at a minimum (Salo et al. 2004). We therefore interpret the peak in the transmission function as indicating the longitude in the rings where the spacecraft is looking directly along the wakes, a geometry that allows the maximum amount of light to pass through the rings.

We use the shape of the transmission function to constrain the properties of the self-gravity wakes. Since wake properties may change with radius, we consider the transmission function in a series of narrow radial bins 20 km wide. Depending on the radius, our occultations provide us either four (126,000–132,000 km) or six (outside 132,000 km) data points for each bin. Given the sparseness of this data set, we cannot make detailed measurements of the shape of the transmission function. Fortunately, numerical models of self-gravity wakes indicate that at these low opening angles, the transmission as a function of longitude can be well approximated by a Gaussian (Salo et al. 2004). We therefore fit the data at each radius to a simple Gaussian model, allowing the amplitude, width, and center of the Gaussian to float. We do not include an additive offset in these fits because there are insufficient degrees of freedom available. Neglecting such a constant term could therefore introduce some errors into the fit, but these errors are expected to be small because the transmission changes by as much as a factor of 8 across the peak. Also, the transmission is predicted to be $<10^{-3}$ away from the peak.

Of the three fit parameters, the longitude of the Gaussian peak has the most straightforward relationship to the wake geometry. The location of the peak corresponds to the longitude at which the most starlight can pass between the wakes, which is

[1] The angle ϕ is also the angle between the line of sight to the star, projected onto the ring plane, and the local radial direction, as defined by Colwell et al. (2006).

determined by the orientation of the wakes ϕ_W relative to the radial direction. Indeed, the longitude of the Gaussian peak relative to the star's position equals the orientation of the wakes relative to the radial direction modulo 180°. As shown in Figure 4 (*top*), the orientation of the self-gravity wakes varies between 66° and 72° throughout the A ring, consistent with numerical wake models (∼69°; Salo et al. 2004) and other measurements of the azimuthal asymmetry from radar observations (67° ± 4°; Nicholson et al. 2005), thermal emission (69° ± 1°; Ferrari et al. 2005), and occultations (57°–66°; Colwell et al. 2006). However, unlike previous observations that measured average wake orientations over extended regions, the o Ceti data also allow us to discern subtle but significant changes in wake orientation with radius. In the middle A ring the orientation is fairly constant at 72°, but it decreases to ∼66° exterior to the Encke Gap. Furthermore, there are two strong dips in ϕ_W at the locations of the two strongest density waves, driven by the Janus 5:4 and Mimas 5:3 inner Lindblad resonances. (There may also be a similar dip at the Janus 6:5 inner Lindblad resonance, but the data here are too noisy to be certain.)

Similar trends can be observed in the peak transmission through the ring (Fig. 4, *middle*). The peak transmission tells us the transmission through the A ring when the wakes are viewed precisely end-on from a point 3.45° above the ring plane. Unfortunately, this parameter is not simply related to any single physical parameter of the self-gravity wakes. If we model the A ring as being composed of an alternating pattern of opaque wakes and partially transparent gaps, the peak transmission $T_{\max}$ will depend on both the opacity of the gaps τ_g and the ratio of the gap width to the wavelength of the wake pattern G/λ:

$$T_{\max} = \frac{G}{\lambda} e^{-\tau_g/\sin B}, \qquad (1)$$

where $B = 3.45°$ is the ring opening angle. Thus, instead of converting the peak transmission into a complicated combination of physical parameters, we simply plot the measured value of $T_{\max}$ itself. As with the wake orientation, we find that the peak transmission is highest in the middle A ring, lowest outside the Encke Gap, and has two broad dips near the same pair of strong density waves (with a more subtle dip at the position of the Janus 6:5 density wave). The broad trends match the variations in azimuthal brightness asymmetry observed in reflected light in *Voyager* images, where the peak asymmetry is seen at a radius of ∼129,000 km (Dones et al. 1993). Our measurements are also consistent with the UVIS estimates of the gap optical depth and wake-to-gap ratios. UVIS finds that τ_g is 0.12 in the middle A ring around 129,000 km, rising to 0.24 outside the Encke Gap, while $G/\lambda = 0.63$ and 0.70 in these two regions (Colwell et al. 2006). The UVIS data would therefore predict $T_{\max} = 0.09$ in the middle A ring and $T_{\max} = 0.015$ outside the Encke Gap, which are comparable to the values in Figure 4.

The similar trends in the wake orientation and peak transmission indicate that both these parameters are sensitive to a common property of the rings, which is most likely the particle size distribution. Numerical simulations show that "small" (centimeter-sized) particles do not aggregate into the self-gravity wakes as readily as do larger, meter-sized particles, so regions with more small particles tend to have more material between the wakes, reducing the peak transmission (Salo et al. 2004). These simulations also show that in regions in which there are more small particles the orientation of the wakes becomes more radial. Both the orientation and the amplitude of the wake signature therefore suggest that there are more small particles in the outer A ring and in the vicinity of the strong density waves than there are in the middle A ring. This is consistent with ground-based occultation data that suggest the particle size distribution in the region outside the Encke Gap extends to smaller sizes than it does elsewhere in the A ring (French & Nicholson 2000).

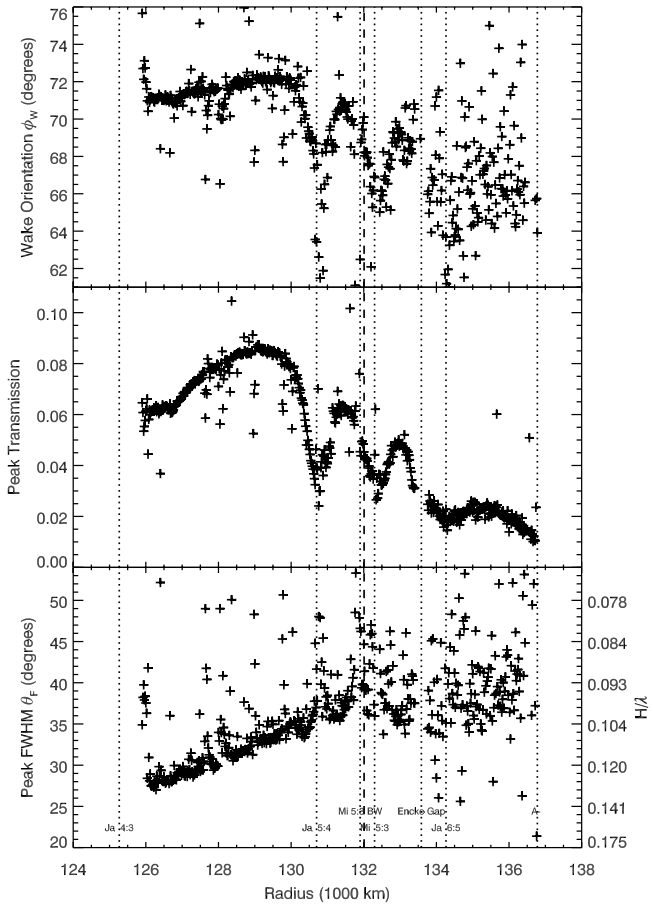

FIG. 4.—Measured wake parameters as a function of radius. The top panel shows the wake orientation, the center panel shows the peak transmission at a 3.45° ring opening angle, and the bottom panel shows the measured peak width and the derived values of the wake height to wake wavelength ratio. Dotted lines show the location of selected features in the A ring, while the dashed line indicates the innermost limit of the orbit 10 occultation. Note there are no discontinuities in the parameters at this location.

The final parameter in our fits is the width of the transmission peak. This parameter does not follow the same trends as the other two, indicating that it is sensitive to different underlying ring properties (see Fig. 4, *bottom*). Indeed, it turns out that for the o Ceti occultations this parameter is most sensitive to the three-dimensional shape of the wakes.

To make this connection concrete, we model the wakes as infinite, straight, parallel, regularly spaced, opaque elliptical cylinders with height H and width W as illustrated in Figure 5. These cylinders are separated by gaps of width G and line-of-sight transmittance $T_g = e^{-\tau_g/\sin B}$. With this simple model, we can calculate the transmission as a function of longitude. If the opening angle of the rings is B and $\theta = \phi - \phi_W$ is the angle between the line of sight and a plane perpendicular to the ring plane and parallel to the wakes, then the transmission $T(\theta)$ is given by

$$T(\theta) = T_g \left[1 - \frac{H \sin\theta}{\lambda \tan B} \sqrt{1 + \left(\frac{W \tan B}{H \sin\theta} \right)^2} \right], \qquad (2)$$

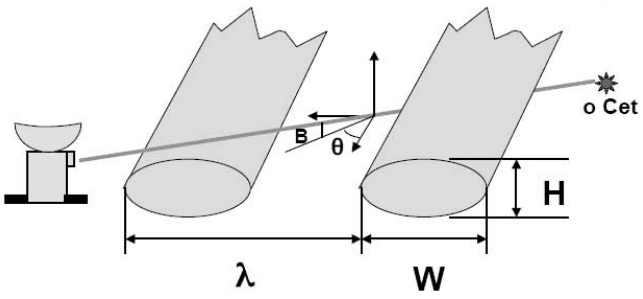

FIG. 5.—Simplified model of the wakes with relevant geometric parameters indicated. [*See the electronic edition of the Journal for a color version of this figure.*]

where $\lambda = W + G$ is the wavelength of the wake pattern. Note that when $\theta = 0$, $T(0) = T_g(1 - W/\lambda) = T_g G/\lambda$, which is equivalent to equation (1), as expected.

This expression is only valid as long as adjacent wakes do not overlap along the line of sight, corresponding to positive values of T. Since overlapping wakes will block all the light from the star, we must set $T = 0$ wherever the above expression for T yields unphysical negative values. Thus, for small values of B the transmission function is sharply peaked around $\theta = 0$ and is only nonzero for values of $|\theta|$ less than a critical value θ_0 where

$$T(\theta_0) \propto 1 - \frac{H \sin\theta_0}{\lambda \tan B}\sqrt{1 + \left(\frac{W \tan B}{H \sin\theta_0}\right)^2} = 0. \quad (3)$$

Since $\theta_0 \sim 30^\circ$ (see Fig. 3) is much larger than $B = 3.45^\circ$ for the o Ceti occultations and H/W is expected to be of order unity (Salo et al. 2004), the term under the square root is approximately 1, and we may approximate θ_0 with the simpler parameter θ_m, defined by the equation

$$\sin\theta_m \equiv \frac{\lambda}{H}\tan B. \quad (4)$$

Since θ_m describes the width of the transmission function in the model, it is directly related to the FWHM of the Gaussian fit θ_F. However, the model transmission function goes to zero at finite θ, while the Gaussian function does not, so the precise relationship between θ_m and θ_F is not obvious. While fitting the above transmission function T to the data would avoid this problem, such a fit would be less robust because of the larger number of free parameters and is therefore not attempted here. Furthermore, we expect that stochastic variations in the wakes would tend to soften the edges of the transmission function and produce a function shaped more like a Gaussian. We therefore use a χ^2-analysis to evaluate the value of θ_F for the Gaussian that best fits a model with a given θ_m. The details of this calculation are presented in the Appendix; the result is that so long as $W/G < 1$ and the model transmission function goes to zero for some values of θ (i.e., $\sin\theta_m < 1$), the FWHM of the Gaussian fit θ_F is within 10% of θ_m. We can therefore approximate

$$\sin\theta_F \simeq \sin\theta_m = \frac{\lambda}{H}\tan B, \quad (5)$$

or, equivalently,

$$\frac{H}{\lambda} \simeq \frac{\tan B}{\sin\theta_F}. \quad (6)$$

The width of the Gaussian fit therefore tells us H/λ, the ratio of the wake height to the wake pattern wavelength. The values of H/λ corresponding to the observed values of θ_F are provided on the right hand side of Figure 4 (*bottom*).

We find that the ratio H/λ is very close to 0.10 through the middle and outer A ring, with only a slight increase across the middle A ring. This implies that the height of the wakes is roughly 10% of the typical wake wavelength throughout the A ring. This is consistent with the UVIS results presented by Colwell et al. (2006). The VIMS and UVIS measurements show somewhat different trends in H/λ across the middle and inner A rings, which are likely due to differences in the analytical methods such as the assumed shapes of the wakes. Given these analytic uncertainties and the relative smallness of the variations ($\sim$20% across the ring), we will not attempt to interpret any trends in H/λ here.

Our estimate of the wake geometry can be converted into a model-dependent estimate of the thickness of the wakes, and perhaps of the A ring itself. The wavelength of the wakes should be set by the Toomre instability length scale λ_T, which is determined by the surface mass density of the ring σ,

$$\lambda_T \simeq 4\pi^2 G\sigma/\Omega^2, \quad (7)$$

where Ω is the orbital angular velocity and G is Newton's constant (Salo et al. 2004). The surface mass density of the A ring has been measured based on its many density waves, which indicate an average of $\sim$40 g cm^{-2} interior to the Encke Gap, and a somewhat lower value in the outermost regions (Spilker et al. 2004; Esposito et al. 1983a; Nicholson et al. 1990; Tiscareno et al. 2007). These measurements indicate that the Toomre length scale is roughly 60 m at a nominal radius of 129,000 km. If we adopt this value, then we find that the wakes are only about 6 m thick. Note that this is a geometric result, not dependent on particle sizes. However, we caution that this estimate of the ring thickness applies only to the larger particles that are strongly clustered into wakelike patterns. There could be a more uniform distribution of smaller particles with a somewhat greater vertical extent. Thus, 6 m should be interpreted as a lower limit on the estimated thickness of the A ring.

4. CONCLUSIONS

Occultations are already providing important constraints on the small-scale texture of the rings. Our estimate of ring thickness suggests that the larger particles are nearly in a monolayer, as expected from numerical simulations (Goldreich & Tremaine 1978; Salo 1995). We also provide the first detailed map of changes in the mean wake orientation with radius, which should provide new insights into how wake properties change with the particle size distribution and the dynamical environment. Future radio and stellar occultation observations at different opening angles and orientations should allow us to better quantify the properties of the self-gravity wakes.

We wish to thank the *Cassini* Project and the VIMS team for their support of this research.

APPENDIX

RELATIONSHIP BETWEEN FIT θ_F AND MODEL θ_m

We fit our data as a function of longitude to a simple Gaussian function of the transmission,

$$T_F(\phi) = Ae^{-(\phi-\phi_W)^2/2\sigma^2}, \quad (8)$$

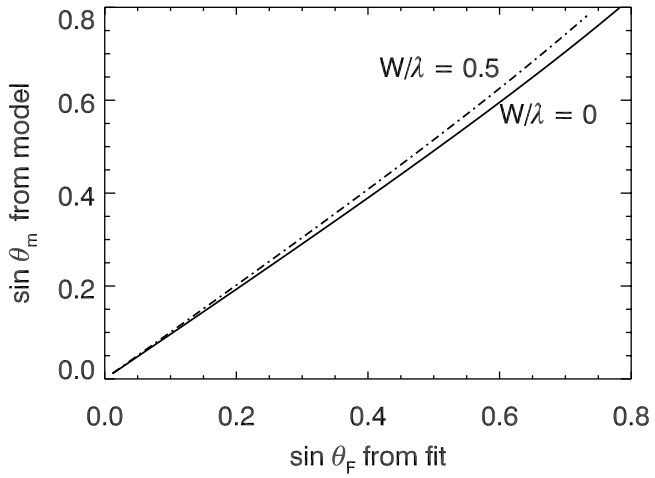

FIG. 6.—Best-fit Gaussian FWHM θ_F as a function of the model θ_m, computed for two values of W/λ. Intermediate values of W/λ fall close to the $W/\lambda = 0$ line

which can also be expressed in terms of the angle $\theta = \phi - \phi_W$,

$$T_F(\theta) = Ae^{-\theta^2/2\sigma^2}. \tag{9}$$

However, in our simple model of infinite, elliptical, regularly spaced wakes, we find the transmission function is given by the function $T_m(\theta)$ given by equation (2), which can be expressed more compactly using the parameter θ_m,

$$\sin\theta_m = \frac{\lambda}{H}\tan B. \tag{10}$$

Using this parameter,

$$T_m(\theta) = \begin{cases} T_g\left[1 - \dfrac{\sin\theta}{\sin\theta_m}\sqrt{1+\left(\dfrac{W\sin\theta_m}{\lambda\sin\theta}\right)^2}\right], & |\theta| < \theta_0 \\ 0, & |\theta| > \theta_0 \end{cases}, \tag{11}$$

where $\sin\theta_0 = [1-(W/\lambda)^2]^{1/2}\sin\theta_m$ defines the maximum θ with nonzero transmission. Note that $\sin\theta_0$ must be less than unity for the signal to approach zero at finite θ, as we observe in Figure 3.

We can relate the parameter θ_m in this model to the σ of the Gaussian fit by finding the Gaussian that best-fits the function $T_m(\theta)$. This is most easily done by minimizing the mean square difference between T_F and T_m, which is given by the integral

$$\chi^2 = \int_0^\infty (T_F - T_m)^2\, d\theta. \tag{12}$$

The minimum of χ^2 occurs where both $\partial\chi^2/\partial A = 0$ and $\partial\chi^2/\partial\sigma = 0$. Since only T_F depends on A and σ, these two equations can be written as

$$\int_0^\infty (T_F - T_m)e^{-\theta^2/2\sigma^2}\, d\theta = 0, \tag{13}$$

$$\int_0^\infty (T_F - T_m)\theta^2 e^{-\theta^2/2\sigma^2}\, d\theta = 0. \tag{14}$$

The terms in these expressions involving T_F are familiar Gaussian integrals and can be evaluated explicitly to give

$$\int_0^\infty T_m e^{-\theta^2/2\sigma^2}\, d\theta = \frac{\sqrt{\pi}}{2}A\sigma, \tag{15}$$

$$\int_0^\infty T_m\theta^2 e^{-\theta^2/2\sigma^2}\, d\theta = \frac{\sqrt{\pi}}{4}A\sigma^3. \tag{16}$$

Combining these expressions to eliminate A, we find

$$\int_0^\infty T_m\left(1 - \frac{2\theta^2}{\sigma^2}\right)e^{-\theta^2/2\sigma^2}\, d\theta = 0. \tag{17}$$

Finally, substituting in the explicit form of T_m (and dividing out T_g), we get

$$\int_0^{\theta_0}\left[1 - \frac{\sin\theta}{\sin\theta_m}\sqrt{1+\left(\frac{W\sin\theta_m}{\lambda\sin\theta}\right)^2}\right]\left(1 - \frac{2\theta^2}{\sigma^2}\right)e^{-\theta^2/2\sigma^2}\, d\theta = 0. \tag{18}$$

If we could evaluate this finite integral explicitly, then we could obtain an expression for σ in terms of θ_m and W/λ. Unfortunately, such an explicit solution is not possible. However, for any given value of θ_m and W/λ, we can numerically compute what value of σ is necessary to make the above integral zero. Figure 6 shows the results of these calculations for $W/\lambda = 0$ and 0.5, which spans the range of values expected for the A ring (Colwell et al. 2006). It turns out that the simple equation $\sin\theta_m = \sin\theta_F$ (where $\theta_F = 2.35\sigma$ is the FWHM of the Gaussian) is a very good approximation (to better than 10%) throughout this range.

REFERENCES

Brown, R. H., et al. 2004, Space Sci. Rev., 115, 111
Colwell, J. E., Esposito, L. W., & Sremcevic, M. 2006, Geophys. Res. Lett., 33, L07201
Dones, L., Cuzzi, J. N., & Showalter, M. R. 1993, Icarus, 105, 184
Esposito, L. W., Ocallaghan, M., & West, R. A. 1983a, Icarus, 56, 439
Esposito, L. W., et al. 1983b, Science, 222, 57
Ferrari, C., et al. 2005, BAAS, 37, 764
Franklin, F. A., Cook, A. F., Barrey, R. T. F., Roff, C. A., Hunt, G. E., & de Rueda, H. B. 1987, Icarus, 69, 280
French, R. G., & Nicholson, P. D. 2000, Icarus, 145, 502
French, R. G., Salo, H., McGhee, C. A., & Dones, L. 2007, Icarus, in press
French, R. G., et al. 1993, Icarus, 103, 163
Goldreich, P., & Tremaine, S. D. 1978, Icarus, 34, 227
Holberg, J. B., Forrester, W. T., & Lissauer, J. J. 1982, Nature, 297, 115
Julian, W. H., & Toomre, A. 1966, ApJ, 146, 810
Lane, A. L., et al. 1982, Science, 215, 537
Lumme, K., & Irvine, W. M. 1984, in IAU Colloq. 75, Planetary Rings, ed. A. Brahic (Toulouse: Depadues-Editions), 87
Nicholson, P. D., Cooke, M. L., & Pelton, E. 1990, AJ, 100, 1339
Nicholson, P. D., French, R. G., Campbell, D. B., Margot, J.-L., Nolan, M. C., Black, G. J., & Salo, H. J. 2005, Icarus, 177, 32
Porco, C., Nicholson, P. D., Borderies, N., Danielson, G. E., Goldreich, P., Holberg, J. B., & Lane, A. L. 1984, Icarus, 60, 1
Salo, H. 1995, Icarus, 117, 287
Salo, H., Karjalainen, R., & French, R. G. 2004, Icarus, 170, 70
Showalter, M. R., Cuzzi, J. N., Marouf, E. A., & Esposito, L. W. 1986, Icarus, 66, 297
Showalter, M. R., & Nicholson, P. D. 1990, Icarus, 87, 285
Spilker, L. J., Pilorz, S., Lane, A. L., Nelson, R. M., Pollard, B., & Russell, C. T. 2004, Icarus, 171, 372
Thompson, W., Vanblerkom, D., & Irvine, W. M. 1984, in IAU Colloq. 75, Planetary Rings, ed. A. Brahic (Toulouse: Depadues-Editions), 93
Tiscareno, M. S., Burns, J. A., Nicholson, P. D., Hedman, M. M., & Porco, C. C. 2007, Icarus, in press